Chemical Science

ROYAL SOCIETY OF CHEMISTRY

EDGE ARTICLE

View Article Online
View Journal | View Issue

Cite this: *Chem. Sci.*, 2025, **16**, 23139

All publication charges for this article have been paid for by the Royal Society of Chemistry

Highly entangled P(VDF-TrFE) solid-state electrolytes for enhanced performance of solid-state lithium batteries

Hanghua Wu,†[a] Shuangfeng Li,†[a] Weiwei Zhu,[b] Jie Zhang,[c] Baohui Ren,*[a] Yan-Fei Huang *[a] and Zhong-Ming Li [de]

Received 27th June 2025
Accepted 20th October 2025

DOI: 10.1039/d5sc04743a

rsc.li/chemical-science

Solid polymer electrolytes (SPEs) offer a promising solution to the safety concerns of lithium metal batteries (LMBs). While poly(vinylidene fluoride) (PVDF)-based SPEs possess advantageous mechanical and thermal properties, their prevalent *trans–gauche* (TGTG) and TTTG conformations create tortuous ion pathways within chains, and insufficient chain entanglement leads to discontinuous transport between chains, fostering non-uniform current distribution and lithium dendrite growth. This work addresses both limitations by employing a novel poly(vinylidene fluoride-*co*-trifluoroethylene), P(VDF-TrFE) copolymer as the matrix of SPEs. By utilizing an ultrahigh molecular weight (2.37×10^6 g mol^{-1}) P(VDF-TrFE) synthesized *via* suspension polymerization, we simultaneously achieve: (1) stabilized TTTT conformation (β-phase), which forms continuous, low-resistance electronegative fluorine channels for efficient intra-chain Li^+ transport, and (2) significantly enhanced chain entanglement density, which establishes a 3D interconnected ion transport network that eliminates inactive microregions, homogenizes Li^+ flux, and improves mechanical resilience. Consequently, Li//Li symmetric cells based on this SPE exhibit exceptional cycling stability exceeding 5000 hours at 0.1 mA cm^{-2} and 25 °C, a 16-fold improvement over a lower molecular weight (0.49×10^6 g mol^{-1}) P(VDF-TrFE) SPE counterpart (~300 hours). $LiNi_{0.8}Co_{0.1}Mn_{0.1}O_2$ (NCM811)//Li full cells also demonstrate good cycling stability. This dual optimization of molecular conformation and topological structure provides an effective strategy for enhancing ion transport continuity and uniformity in solid-state LMBs.

1. Introduction

Solid-state electrolytes (SSEs) could be used to replace liquid electrolytes to address the safety issue of lithium metal batteries (LMBs).[1,2] Among various SSEs, polymeric SSEs (SPEs) stand out for their high flexibility, easy scalability, and low cost.[3–5] Up to date, several SPEs have been developed, including those based on poly(ethylene oxide), poly(methyl methacrylate), polyacrylonitrile, poly(vinylene carbonate), and poly(vinylidene fluoride) (PVDF).[6–10] Among these, PVDF-based SPEs are distinguished by their relatively high mechanical strength, excellent thermal stability, and broad electrochemical stability window compared to other SPEs.[11] However, conventional PVDF-based SPEs tend to adopt *trans–gauche* (TGTG) and TTTG conformations, where fluorine (F) atoms are arranged on both sides of the carbon chain.[12] This makes the ion hopping path along the F atoms rather tortuous (Fig. 1a), resulting in low ions transport efficiency within polymer chains.[13] More critically, PVDF-based SPEs tend to form porous architectures with discontinuous ion transport pathways between polymer chains (Fig. 1b), primarily due to insufficient mutual contact between polymer chains (known as chain entanglement). This structural deficiency results in non-uniform current distribution throughout SPEs,[14] easily triggering the growth of lithium dendrites that lead to premature failure of LMBs.[15,16]

To enhance the ordered arrangement of F atoms in PVDF, the core strategy lies in transforming the TGTG (α phase) and TTTG (γ phase) conformations into the all-*trans* (TTTT) conformation (β phase), where F atoms align uniformly on the same side of the carbon chain. In recent years, researchers have effectively induced TTTT conformation in PVDF-based SPEs through approaches such as incorporating inorganic fillers,[17–19] modulating solvent polarity,[20,21] and optimizing crystallization conditions.[22] For instance, Kang *et al.* demonstrated that adding

[a]*Guangdong Provincial Key Laboratory of New Energy Materials Service Safety, Shenzhen Key Laboratory of Polymer Science and Technology, College of Materials Science and Engineering, Shenzhen University, Shenzhen 518055, P. R. China. E-mail: yanfeihuang@szu.edu.cn; renbaohui@szu.edu.cn*

[b]*Zhejiang Chemical Industry Research Institute Co., Ltd, Hangzhou, 310023, China*

[c]*College of Polymer Science and Engineering, State Key Laboratory of Polymer Materials Engineering, Sichuan University, Chengdu 610065, P. R. China*

[d]*West China Hospital/West China School of Medicine, Sichuan University, Chengdu 610041, China*

[e]*State Key Laboratory of Advanced Polymer Materials, Sichuan University, Chengdu 610065, China*

† These authors contribute equally to this work.

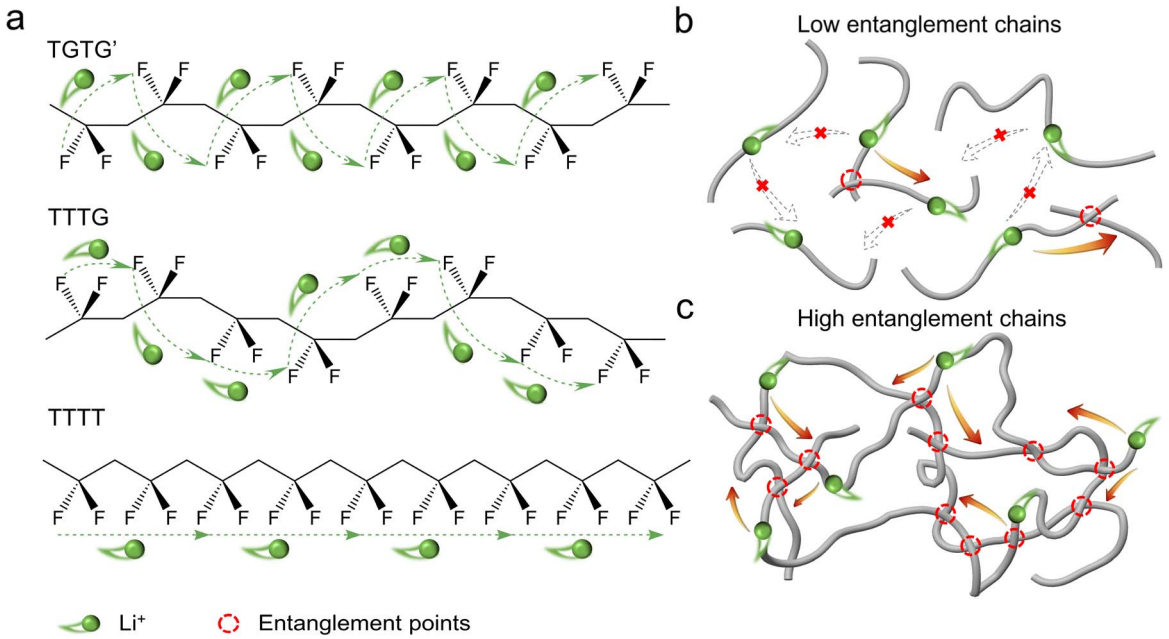

Fig. 1 (a) Schematic diagram of ion transport of PVDF-based polymers with different conformations. Intermolecular chain ion transport of (b) low entanglement molecular chains and (c) high entanglement molecular chains.

13 wt% dielectric $NaNbO_3$ filler increased the TTTT conformation content in PVDF SPEs from 40.5% to 63.9%, significantly improving ionic conductivity.[23] However, existing methods still face challenges such as poor filler dispersion, complex processes, and incomplete conversion of TGTG and TTTG conformations. Developing novel techniques to achieve full conformational conversion remains a critical challenge in this field.

Notably, poly(vinylidene fluoride-*co*-trifluoroethylene) [P(VDF-TrFE)] copolymers containing 18–50 mol% TrFE monomers exhibit unique advantages in applications such as film capacitors,[24–26] as their low-temperature cooling phase spontaneously forms molecular chains with TTTT conformation.[27,28] However, commercially available P(VDF-TrFE) materials typically have a molecular weight of approximately 0.45 million (M) g mol^{-1},[12,29] far below the industrial PVDF binders for LMBs (1 M g mol^{-1}).[30–32] This low molecular weight results in insufficient polymer chain entanglement density, severely impairing the continuous transport of lithium ions between polymer chains. Furthermore, the extremely low flash point of TrFE monomers necessitates the use of explosion-proof autoclaves and on-site monomer production facilities during copolymer synthesis.[33] These stringent requirements greatly limits the feasibility of increasing the molecular weight of P(VDF-TrFE), and puts the technological path to improve the chain entanglement density in a difficult situation.

It was reported that chain entanglement constructed through strategies such as interpenetrating networks, nanofillers, and nanoconfinement can improve battery performance.[34–36] For example, Xia *et al.* reported that entangled poly(vinylidene fluoride-*co*-hexafluoropropylene) electrolyte effectively mitigates dendrite-induced stress during cycling and facilitates the formation of a stable interface layer, thereby enhancing battery performance.[34] In addition, Lu *et al.* demonstrated functionalizing the ordered pores of covalent organic frameworks with initiators can regulate the chain entanglement of poly(1,3-dioxolane) polymer, leading to both enhanced electrochemical stability and fire safety.[35] However, these ways to introducing chain entanglement fail to take into account the regulation of the molecular chain conformation of PVDF.

In this study, a P(VDF-TrFE) copolymer with ultrahigh weight-averaged molecular weight (M_w) of 2.37 M g mol^{-1} is synthesized *via* suspension free radical copolymerization, and is first employed to construct a novel SPE system, which combines conformational ordering and dense chain entanglement. The TTTT conformation of P(VDF-TrFE) chains facilitates the formation of continuous electronegative F atom channels, creating low-resistance pathways for lithium-ion conduction (Fig. 1a). More importantly, the enhanced chain entanglement density establishes a three-dimensional interconnected ion transport network, which minimizes inactive microregions and thereby homogenizes Li^+ flux to suppress lithium dendrite growth (Fig. 1c). As a result, the Li//Li symmetric cell based on the highly entangled P(VDF-TrFE)-2.37 M SPE exhibits impressive cycling stability over 5000 hours at 0.1 mA cm^{-2} at 25 °C, representing a 16-fold improvement compared that (~300 h) of the controlled Li//Li cell based on a less entangled P(VDF-TrFE) SPE (M_w = 0.49 M g mol^{-1}). Moreover, the $LiNi_{0.8}Co_{0.1}Mn_{0.1}O_2$ (NCM811)/P(VDF-TrFE)-2.37 M SPE/Li full cells also present good cycling stability at 25 °C. This study collectively addresses critical challenges in ion transport continuity and spatial uniformity for solid-state LMBs by simultaneously optimizing the molecular conformation and topological structure.

2. Results and discussion

In general, the entanglement density of polymer systems exhibits a proportional relationship with molecular weight.[37] Guided by this principle, P(VDF-TrFE) copolymers with molecular weight ranging from 0.49 M to 2.37 M g mol^{-1} (Fig. S1, S2 and Table S1) were synthesized in this study, and the corresponding SPEs were prepared by solution casting following an optimized procedure reported in our previous work.[12,38] Small-amplitude oscillatory shear (SAOS) rheology measurements at different temperatures were employed to determine the entanglement number (Z). As shown in Fig. 2a and S3, the obtained results were fitted by time–temperature superposition (TTS) principle at the reference temperature of 200 °C to obtained the platform modulus (G_N^0). From equations, $Z = M_w/M_e$, and $M_e = \rho RT/G_N^0$ (M_e the entangled molecular weight, ρ the density, R the ideal gas constant, and T the thermodynamic temperature), the M_e and Z were calculated as shown in Fig. 2b. It is shown that the number of entanglements of P(VDF-TrFE)-2.37 M is 109.9, which is more than 3 times of that of P(VDF-TrFE)-0.49 M (Z = 36.3), indicating that the interacting molecular chains in the entangled region of the polymer as well as the overall density of the entanglements are increased. From Fourier transform infrared (FTIR) measurement (Fig. 2c), all P(VDF-TrFE) electrolytes exhibit distinct characteristic peaks at 470 cm^{-1}, 840 cm^{-1}, and 1280 cm^{-1}, indicating that the molecular chains adopt an TTTT conformation. This conformation is highly polar to facilitate the dissociation of lithium salts,[12] and creates connected electronegative channels for fast ions transport (Fig. 1a).[11] Furthermore, X-ray diffraction (XRD) analysis (Fig. S4) and wide-angle X-ray scattering (WAXS) results (Fig. 2d–f) reveal that P(VDF-TrFE) with different molecular weights exhibits pure ferroelectric (FE) phase, which corresponds to TTTT conformation. From differential scanning calorimetry (DSC) results (Fig. 2g), the Curie transition temperature (T_c) of all samples are much higher than 25 °C, proving again the P(VDF-TrFE) shows a pure FE phase at room temperature.[39] Additionally, the peak intensity of T_c decreases with the increase of molecular weight of P(VDF-TrFE), indicating that the P(VDF-TrFE) with higher molecular weight shows a smaller FE domain size. Such small FE domain is believed to show a higher ability to rotate than large domains under electrical field,[40] which probably can facilitate ions transport through ion–dipole interactions. In SPEs, Li^+

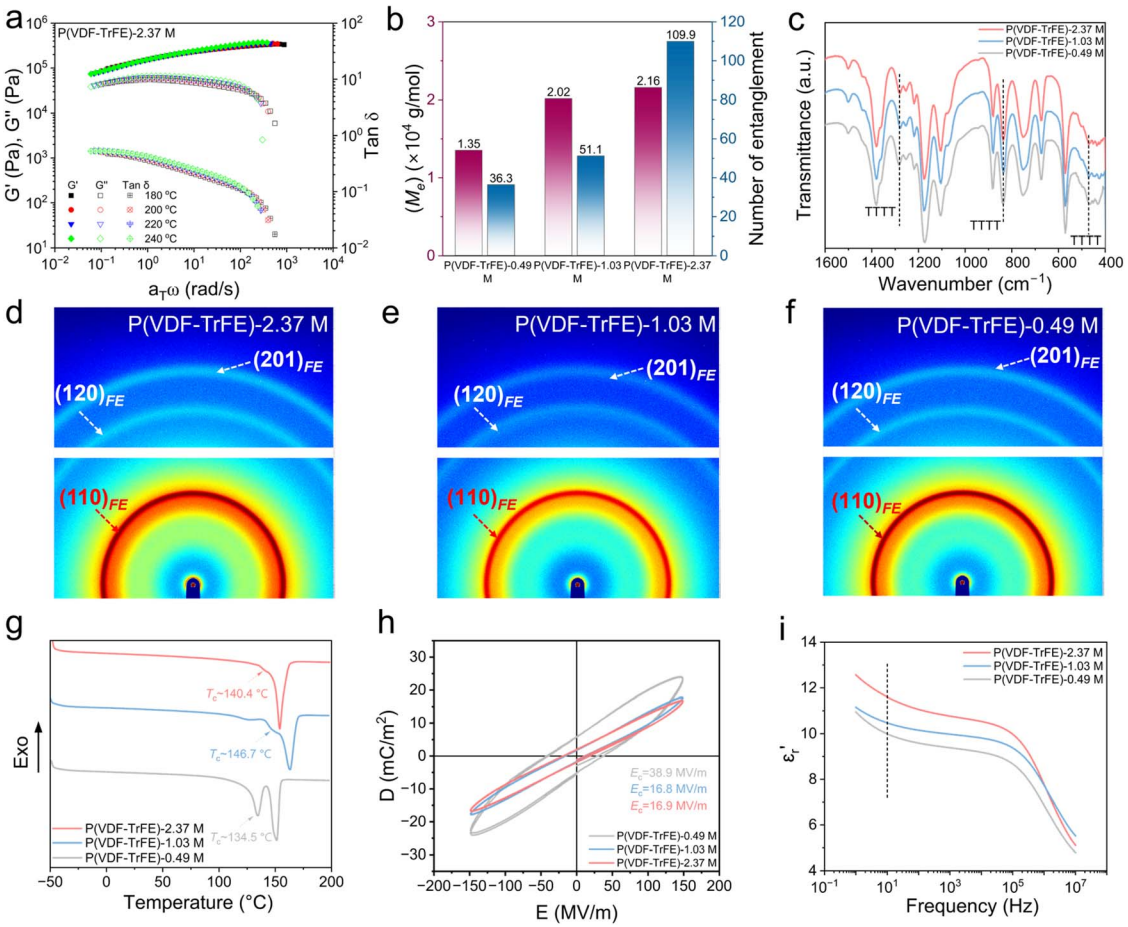

Fig. 2 (a) Time–temperature superposition curves of P(VDF-TrFE)-2.37 M shifted to a reference temperature of 200 °C. (b) M_e and number of entanglement, (c) FTIR curves, (d)–(f) WAXS spectrum, (g) DSC heating curves, (h) bipolar D–E loops, and (i) BDS spectrum of P(VDF-TrFE) with different molecular weights.

transport is generally understood to occur primarily through segmental motion and relaxation in the amorphous regions of the polymer matrix.[41] Therefore, a higher proportion of the amorphous phase, *i.e.*, lower crystallinity, typically enhances ion transport capability.[42] To further quantify the crystallinity of P(VDF-TrFE) SPEs with different molecular weights, XRD spectra were deconvoluted through peak fitting analysis. As shown in Fig. S5, the crystallinity of P(VDF-TrFE) SPE decreases with increasing molecular weight, dropping from 39.1% for P(VDF-TrFE)-0.49 M to about ~34% for P(VDF-TrFE) with higher molecular weight (1.03 and 2.37 M g mol^{-1}). This reduction is likely due to the decreased chain flexibility due to the increased number of chain entanglement points, which inhibits partial crystallization as proved by DSC cooling curves (Fig. S6), where the higher the molecular weight of the polymer, the lower the crystallization temperature and the smaller the crystallization enthalpy. From displacement–electric field (*D*–*E*) measurements, the coercive field (E_c) decreases with the increasing of molecular weight (Fig. 2h). This suggests a corresponding reduction in FE domain size within the P(VDF-TrFE) copolymer, correlating well with DSC results. Broadband dielectric spectroscopy (BDS) was employed to measure the relative dielectric constant (ε_r) of different P(VDF-TrFE). It is shown that the higher the molecular weight of P(VDF-TrFE), the greater the ε_r (Fig. 2i). This is probably because the high entanglement hinders the crystallization, resulting in a smaller FE domain size for P(VDF-TrFE) with higher molecular weight (Fig. 2g and h). As reported,[43,44] the decreased FE domain size make it easier for dipoles to rotate under electrical field. This results in a higher ε_r for highly entangled P(VDF-TrFE). The enhanced ε_r facilitates more efficient dissociation of lithium salts into free charge carriers, thereby would probably improve ionic conductivities.[38]

Scanning electron microscopy (SEM) was employed to observe morphologies of different SPEs. As shown in Fig. 3a–c, P(VDF-TrFE) SPEs with higher M_w (1.03, 2.37 M g mol^{-1}) show relatively denser morphology than that with lower M_w (0.49 M g mol^{-1}), leading to a thinner thickness (Fig. 3d–f). This is probably highly related to the high molecular chain entanglement density that enhances intermolecular interactions and contributes to a denser morphology. Such structure may endow the SPE with higher potential to inhibit lithium dendrite growth and thus enhance the cycling stability. From electrochemical impedance spectroscopy (EIS) measurements (Fig. S7), the P(VDF-TrFE)-2.37 M SPE exhibits slightly lower ionic conductivity than its low M_w counterparts (0.49 M and 1.03 M) at room temperature (Fig. 3g), yet outperforms them at elevated temperatures. This probably stems from molecular weight-dependent chain entanglement and intensified intermolecular forces at different temperatures. At room-temperature, the high entanglement restrict segmental mobility and consequently suppress ion transport through segment-assisted diffusion mechanisms.[45] As a result, the P(VDF-TrFE)-2.37 M SPE shows a slightly decreased ionic conductivity from 7.10×10^{-4} S cm^{-1} for P(VDF-TrFE)-0.49 M SPE to 5.78×10^{-4} S cm^{-1}. However, the value of 5.78×10^{-4} S cm^{-1} is quite high compared to conventional PVDF SPEs reported in literature,[46,47] and is adequate for enabling LMBs to exhibit good cycling stability. At elevated temperatures, polymer chains undergo partial disentanglement. For low-M_w electrolytes (0.49 M) with inherently sparse entanglement, this thermal disentanglement further increases interchain spacing, severely impeding ion transport between polymer chains (Fig. 1b). In contrast, high-M_w electrolytes (2.37 M) retain sufficient residual entanglement to maintain closer interchain proximity, thereby preserving continuous ion transport pathways (Fig. 1c). Consequently, P(VDF-TrFE)-2.37 M SPE exhibit superior ionic conductivity compared to their low-M_w counterparts under high-temperature conditions. EIS measurement also gives the ion migration activation energy (E_a), and it is 0.236 eV for P(VDF-TrFE)-2.37 M SPE, although slightly higher than other SPEs but adequate for fast ions transport according to literatures.[48,49] The pulsed-field gradient NMR (PFG-NMR) measurements show that P(VDF-TrFE)-2.37 M (2.650×10^{-11} m^2 s^{-1}) displays slightly larger Li^+ diffusion coefficients than P(VDF-TrFE)-1.03 M (2.624×10^{-11} m^2 s^{-1}) and P(VDF-TrFE)-0.49 M (2.221×10^{-11} m^2 s^{-1}) (Fig. S8). Theoretically, the ion transport in SPE occurs through the transmission of Li^+ within the molecular chains and between the molecular chains, as schematically shown in Fig. 1. Since chain entanglement hinders segmental motion, the transmission of Li^+ within the molecular chains should be hindered for highly entangled P(VDF-TrFE)-2.37 M. However, the P(VDF-TrFE)-2.37 M shows a slightly higher Li^+ diffusion coefficients. This suggests that the transmission of Li^+ between molecular chains (*i.e.* hopping from one molecular to another) are greatly improved for P(VDF-TrFE)-2.37 M, making it much faster than that for low entangled P(VDF-TrFE)-0.49 M. Owing to enhanced Li^+ transmission rate between molecular chains, we believe that the difference in ionic transmission within molecular chains and between molecular chains has been narrowed. In other words, the chain entanglement homogenizes Li^+ flux. With increased overall Li^+ diffusion coefficient, entangled SPE ($M_w = 2.37$ M) has lower ionic conductivity (5.78×10^{-4} S cm^{-1}) *vs.* low-M_w SPE at 25 °C. This is probably because the high-M_w P(VDF-TrFE) show lower polarity than low-M_w P(VDF-TrFE) (Fig. 2h), which reduces the ability of P(VDF-TrFE) matrix to dissociate lithium salts into free ions.[12] Li^+ transference number (t_{Li^+}) measurements show that t_{Li^+} are comparable across different molecular weights, with values of 0.29 for P(VDF-TrFE)-0.49 M, 0.23 for P(VDF-TrFE)-1.03 M, and 0.27 for P(VDF-TrFE)-2.37 M (Fig. S9). These results suggest that while molecular chain entanglement influences the overall ionic conductivity, it does not substantially alter the selective transport of ions during conduction.

Thermogravimetric analysis (TGA) was conducted to investigate the residual *N*,*N*-dimethylformamide (DMF) content in P(VDF-TrFE) electrolytes with different molecular weights. As shown in Fig. 3h, a slight weight loss was observed before 55 °C, which can be attributed to the evaporation of absorbed moisture. The weight loss in the temperature range of 55 °C to 200 °C corresponds to the removal of residual DMF solvent. Based on the TGA curves, the residual DMF content in P(VDF-TrFE)-2.37 M, P(VDF-TrFE)-1.03 M, and P(VDF-TrFE)-0.49 M electrolytes is calculated to be 22.68%, 16.86%, and 15.31%,

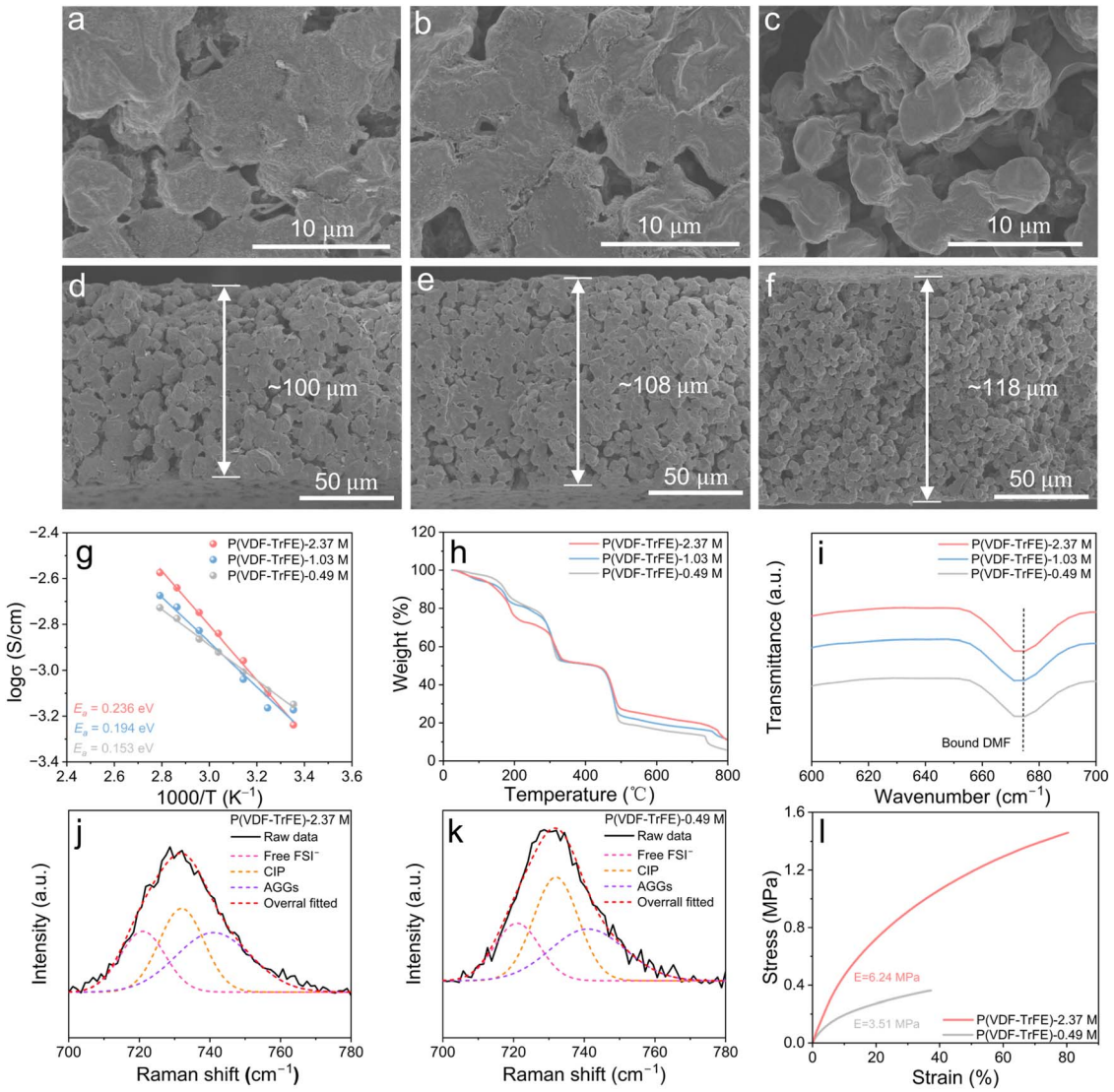

Fig. 3 Cross-sectional SEM images of (a) and (d) P(VDF-TrFE)-2.37 M, (b) and (e) P(VDF-TrFE)-1.03 M, and (c) and (f) P(VDF-TrFE)-0.49 M at different magnifications. (g) Ionic conductivities of P(VDF-TrFE) with different molecular weights at different temperature. (h) TGA, and (i) FTIR curves in the range of 600–700 cm^{-1}, (j) and (k) Raman spectrum spectra in the range of 700–780 cm^{-1} and (l) stress–strain curves of P(VDF-TrFE) electrolytes with different molecular weights.

respectively. From FTIR (Fig. 3i) and Raman spectroscopy (Fig. S10), only peaks for bound DMF exist,[50] suggesting that all prepared P(VDF-TrFE) electrolytes are still in solid state. The higher DMF residue in P(VDF-TrFE)-2.37 M is probably because the much denser entanglement network helps to absorb more DMF. With higher residual DMF content, P(VDF-TrFE)-2.37 M SPE shows a slightly lower ionic conductivity than other samples, demonstrating again it contains large amounts of entanglements that limits the chain segments motion for ions transport. To exclude the influence of residual DMF on polymer chain segmental motion, the ion conductivity of P(VDF-TrFE)-2.37 M SPEs with similar DMF residue (~16.1%) with P(VDF-TrFE)-0.49 M was measured, and it further reduces to around ~4.02×10^{-4} S cm^{-1} (Fig. S11 and Table S2). Moreover, DFT result shows that DMF would slightly loosen the entanglement of P(VDF-TrFE), with a more pronounced impact on low M_w system (Fig. S12). Furthermore, Raman test was employed to explore the ionic coordination environments in P(VDF-TrFE) SPE with different entanglement density. The FSI^- (S–N–S) anion peaks at 735 cm^{-1} are deconvoluted into three distinct ion coordination states according literatures: free FSI^- (SSIP), contact ion pairs (CIP), and aggregates (AGGs) (Fig. 3j and k).[51,52] The CIP and AGG corresponds to FSI^- coordinated with a single Li^+ and interacting with two or more Li^+. The fraction of AGG is 40.7% for the P(VDF-TrFE)-2.37 M SPE, which is much higher than that (34.8%) of the P(VDF-TrFE)-0.49 M SPE. Such difference may be attributed to the varied chain entanglements that changes the ion coordination environment. As reported, the AGG form helps to form fast ion transport channels,[53] which can partially counteract the hindrance caused by high entanglement on the ions transport. This explains the P(VDF-TrFE)-

2.37 M SPE with 202.8% higher entanglement density only shows slightly (18.6%) lower ionic conductivity at 25 °C.

Tensile tests were conducted to assess the impact of chain entanglements on the mechanical properties of the SPEs. As shown in Fig. 3l, the highly entangled P(VDF-TrFE)-2.37 M SPE shows a high tensile strength of 1.46 MPa and Young's modulus of 6.24 MPa, significantly surpassing 0.35 MPa and 3.51 MPa of the less entangled P(VDF-TrFE)-0.49 M SPE. A similar trend was observed in the elongation at break, where P(VDF-TrFE)-2.37 M SPE (~80%) substantially outperform the P(VDF-TrFE)-0.49 M (37%). These results indicate that P(VDF-TrFE) electrolyte films with higher chain entanglement density exhibit stronger intermolecular forces to resist external forces, leading to superior mechanical strength and excellent toughness, which is of great beneficial to suppress lithium dendrite growth and improve the cycling stabily of solid-state LMBs.[54–56]

To elucidate the role of polymer chain entanglement in Li^+ transport continuity and uniformity, we assembled Li//Li symmetric cells using P(VDF-TrFE) SPEs with different molecular weights and evaluated their cycling stability. As shown in Fig. 4a, P(VDF-TrFE) SPEs with higher entanglements exhibit lower polarization voltage and longer cycling lifetimes at current densities of 0.1, 0.2, and 0.3 mA cm^{-2} at 25 °C. Notably, P(VDF-TrFE)-2.37 M demonstrates exceptional cycling stability, operating stably for over 5000 h at 0.1 mA cm^{-2} and 25 °C without short-circuiting and maintaining a low polarization voltage of 72 mV (Fig. 4a). In contrast, P(VDF-TrFE)-1.03 M electrolyte undergoes short-circuit failures at 2942 h, and P(VDF-TrFE)-0.49 M fails within just only 225 h (Fig. 4a). At a higher current density of 0.2 mA cm^{-2}, the cell based on P(VDF-TrFE)-2.37 M SPE remains stable for over 700 h, while cells based on P(VDF-TrFE)-1.03 M and P(VDF-TrFE)-0.49 M SPEs short-circuit after 450 h and 98 h, respectively (Fig. 4b). Surprisingly, even at 0.3 mA cm^{-2}, P(VDF-TrFE)-2.37 M still exhibits remarkable stability, maintaining stable cycling for over 600 h (Fig. 4c). The improved cycling stability is attributed to the high entanglement density of P(VDF-TrFE)-2.37 M, which assures uniform ions transport throughout the SPE (Fig. 1c) and then inhibits the dendrite growth. Next, Li/P(VDF-TrFE)/Cu half cells with different molecular weights were investigated to assess the coulombic efficiency (CE) of the corresponding SPEs (Fig. S13). The CE of P(VDF-TrFE)-2.37 M reaches 96.26%, which is significantly higher than those of P(VDF-TrFE)-1.03 M and P(VDF-TrFE)-0.49 M. Since the modulus of SPEs is also an important factor in preventing the dendrite growth,[57] a P(VDF-TrFE)-0.60 M SPE with similar modulus with P(VDF-TrFE)-0.49 M SPE (Fig. S14) was prepared to explore the mechanical enhancement on dendrite suppression. It is shown that the Li/P(VDF-TrFE)-0.60 M SPE/Li cell performs much better than Li/P(VDF-TrFE)-0.49 M SPE/Li at varied current densities although these SPEs show comparable modulus. This confirms again the increased chain entanglement density helps to inhibit dendrite growth, probably because of more connected ions transport pathway brought by increased entanglement points (Fig. 1c). Additionally, as shown in Fig. 4d, the critical current density (CCD) of P(VDF-TrFE)-2.37 M reaches 0.70 mA cm^{-2}, which is more than twice the CCD of P(VDF-TrFE)-0.49 M (0.35 mA cm^{-2}). This further proves the positive role of high entanglement on preventing the dendrite growth.

To further evaluate the interfacial stability of the Li/P(VDF-TrFE)/Li cells during cycling, EIS measurements were performed before and after cycling (Fig. 4e–h). As for P(VDF-TrFE)-0.49 M, the interfacial impedance decreases rapidly from 205 Ω to 29 Ω after 160 cycles, but then increasing to 36 Ω after 200 cycles. The increase of impedance after cycling is probably due to some side reactions, which explains the short cycling life the Li/P(VDF-TrFE)-0.49 M/Li cell. In contrast, the P(VDF-TrFE)-2.37 M exhibits a gradual and steady decrease in interfacial resistance even after 400 cycles, suggesting the formation of a stable solid-state electrolyte interphases (SEI) that enhances interfacial compatibility. Moreover, post-cycling lithium metal surface morphology analysis (Fig. S15) reveals that P(VDF-TrFE) electrolytes with higher molecular weights have a significantly smoother and more uniform lithium deposition, whereas lower molecular weight electrolytes lead to severe dendrite growth and pore formation. This can be attributed to insufficient polymer chain entanglement in low M_w-P(VDF-TrFE), which results in porous, ion-blocking microdomains that hinder uniform Li^+ transport (Fig. 1b), ultimately leading to dendritic growth. Conversely, higher M_w-P(VDF-TrFE) possesses a denser polymer matrix with enhanced chain entanglement, ensuring more continuous and flexible Li^+ transport pathways, thereby promoting uniform ion distribution and suppressing dendrite formation (Fig. 4i and j). To assess whether residual DMF changes after cycling and whether it causes any long-term instability or side reactions, we measured the residual DMF in Li//Cu cells before and after cycling using TGA. As demonstrated in Fig. S16a, the amount of residual DMF was reduced from 20.0% to 17.0%, which indicates partial consumption during cycling. Importantly, FTIR analyses (Fig. S16b) showed no characteristic absorption of conjugated –CH=CF– double bonds caused by free radicals by electron transfer between DMF and a Li foil.[58] This indicates that P(VDF-TrFE)-2.37 M was not dehydrofluorinated and no HF was released. Therefore, it may be deduced that residual DMF does not induce side reactions or compromise the long-term cycling stability of the cells. We further performed DFT calculations to visualize Li^+ transport. As shown in Fig. S17, the energy barrier for interchain transport in higher-M_w P(VDF-TrFE) (−0.109 eV) is lower than that in the lower-M_w counterpart, indicating that increased chain entanglement indeed facilitates more efficient Li^+ interchain transfer. This would narrow the gap between the transfer rates of ions within (*i.e.* intramolecular) and between (*i.e.* intermolecular) molecular chains, thus contributing to a more uniform Li^+ flux.

In summary, there is a trade-off between entanglement, conductivity, and cycling stability that contributes to the prolonged cycling stability of high-M_w P(VDF-TrFE) SPE. Specifically, at room temperature, the highly entangled P(VDF-TrFE)-based SPEs restrict segmental mobility and consequently suppress ion transport through segment-assisted diffusion, resulting in lower ionic conductivity. However, the dense entanglement network enhances intermolecular interactions, which provides additional accessible sites and alternative pathways for Li^+ transport. Such characteristics facilitate a more

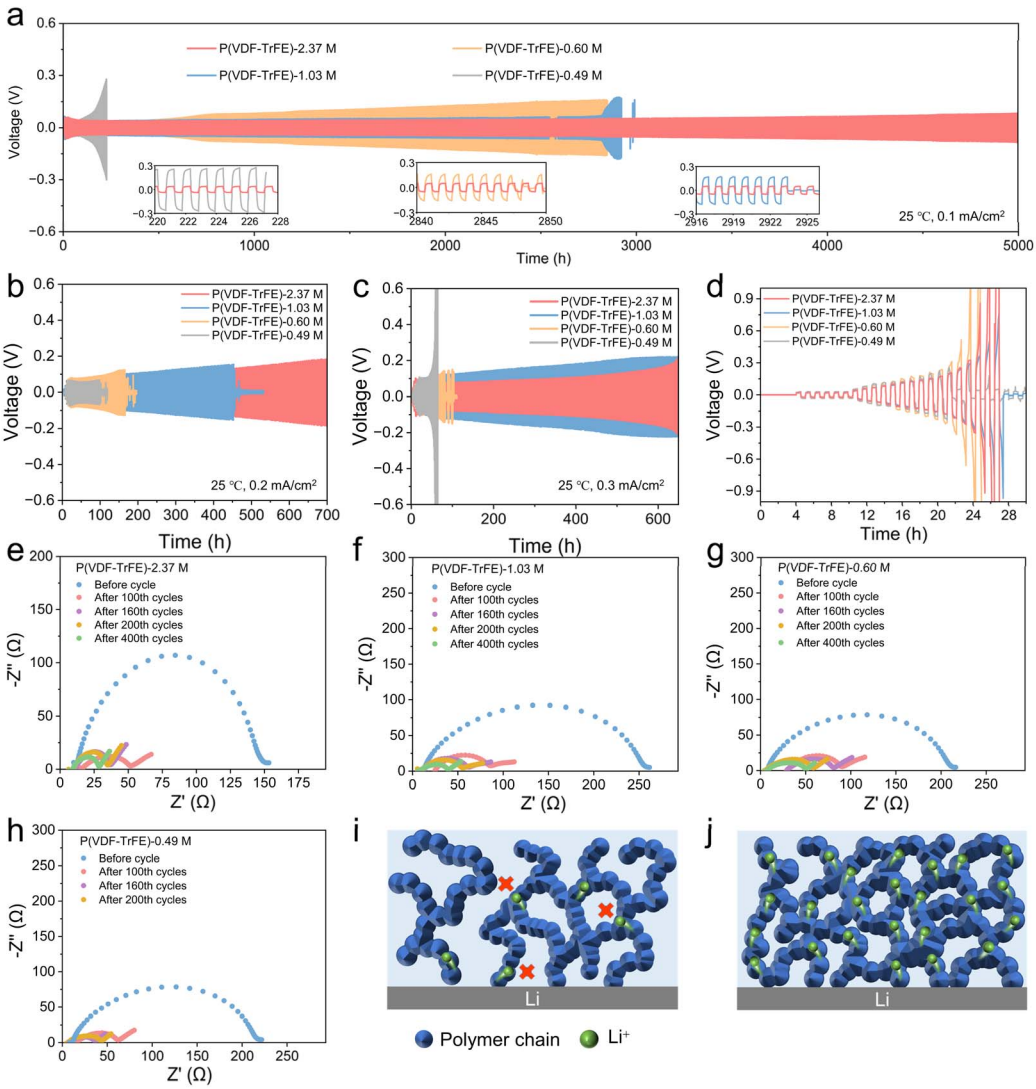

Fig. 4 (a) Cycling profiles of the Li/P(VDF-TrFE) SPEs/Li symmetric cell at 25 °C under 0.1 mA cm^{-2}. The insets show voltage profiles for around 220, 2840, and 2916 h. Cycling performance of the Li/P(VDF-TrFE) SPEs/Li symmetric cell at 25 °C under (b) 0.2 mA cm^{-2} and (c) 0.3 mA cm^{-2}. (d) CCD of the electrolytes at 25 °C. (e)–(h) EIS spectra of the Li/P(VDF-TrFE) SPEs/Li symmetric cells after 100, 160, 200, and 400 cycles. Schematic diagram of (i) low entanglement molecular chains and (j) high entanglement molecular chains near Li anodes.

uniform Li^+ flux and more homogeneous Li^+ deposition/stripping at the electrode interface. As confirmed by SEM analysis, fewer dendrites form in the highly entangled P(VDF-TrFE)-2.37 M SPE (Fig. 3a–f), leading to long-term cycling stability. Moreover, the strong intermolecular forces endow the highly entangled SPE with enhanced mechanical properties. Specifically, the P(VDF-TrFE)-2.37 M SPE exhibits a tensile strength of 1.46 MPa, a Young's modulus of 6.24 MPa, and an elongation at break of ~80%, all significantly higher than its low-M_w counterpart. Such mechanical strength helps the electrolyte accommodate electrode volume changes and resist physical stresses, thereby further mitigating dendrite formation and contributing to stable cycling.

To further evaluate the practical potential of the assembled cells, SS//Li batteries were fabricated to measure the electrochemical stability window. From linear sweep voltammetry (LSV) test (Fig. 5a and S18), the P(VDF-TrFE)-2.37 M SPE exhibits the broadest electrochemical stability window, exceeding 4.7 V. In contrast, P(VDF-TrFE)-0.49 M show significant current rise before 4.0 V, with current values reaching 8 μA at 4.2 V. This enhanced electrochemical stability for higher molecular weight polymers can be also attributed to the greater chain strength and higher degree of polymer entanglement, which enhances the structural integrity of the polymer matrix. To further assess the compatibility of the P(VDF-TrFE) electrolyte with high-voltage cathodes, cycling performance tests were conducted on NCM811/P(VDF-TrFE)/Li cells. As illustrated in Fig. 5b, under a charge/discharge rate of 0.5C at 25 °C, the NCM811/P(VDF-TrFE)-2.37 M/Li battery retains 82.2% of its initial capacity after 300 cycles, which is superior to that of P(VDF-TrFE)-0.49 M (78.3%). Additionally, after 350 cycles, P(VDF-TrFE)-2.37 M maintains a coulombic efficiency of over 99%,

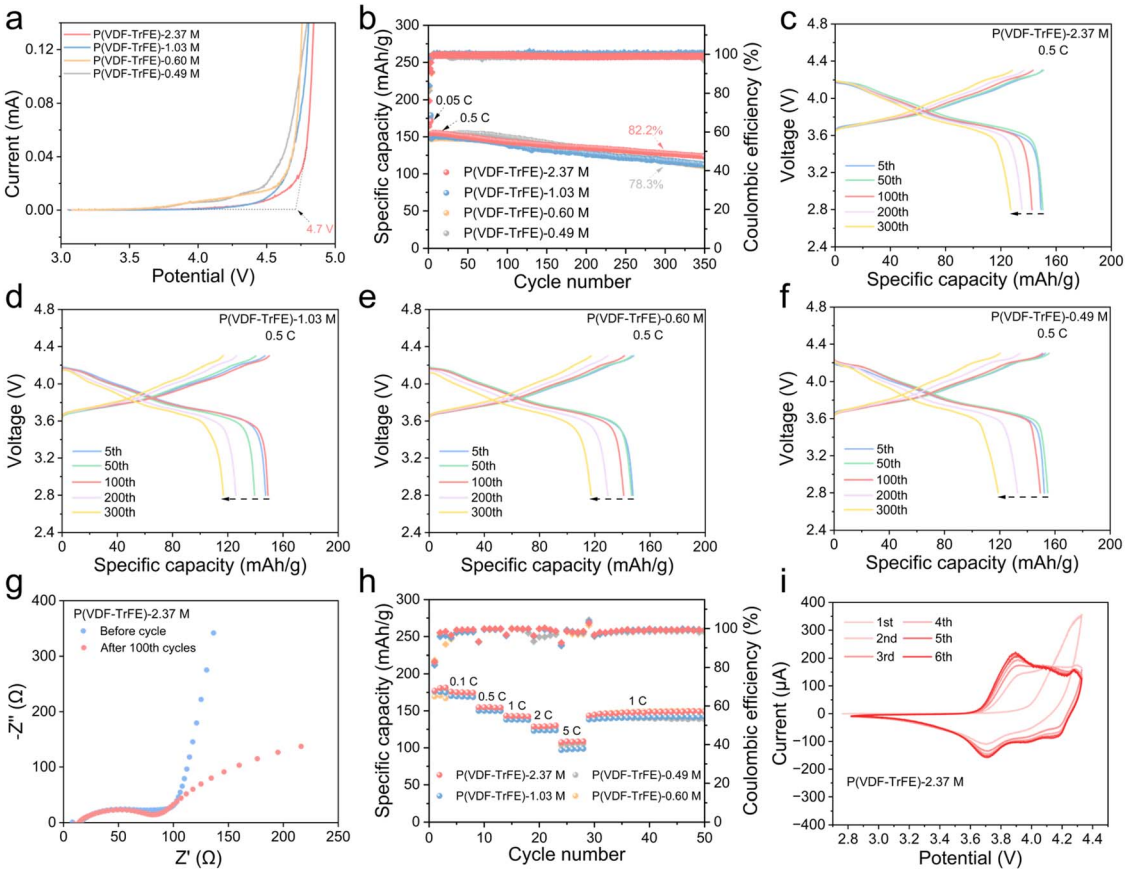

Fig. 5 (a) LSV test, (b) cycling performance, and (c)–(f) charge/discharge curves of NCM811/P(VDF-TrFE) SPEs/Li full cells with different molecular weights at 0.5C. (g) EIS spectra of the NCM811/P(VDF-TrFE) SPEs/Li full cell before and after 100 cycles. (h) Rate performance of the NCM811/P(VDF-TrFE) SPEs/Li full cells. (i) CV curves of P(VDF-TrFE)-2.37 M.

indicating excellent cycling stability of NCM811/P(VDF-TrFE) SPEs/Li cells. Fig. 5c–f presents the charge–discharge profiles of NCM811/P(VDF-TrFE) SPEs/Li cells with different molecular weight electrolytes at various cycle numbers. Within the initial 50 cycles, all four cells exhibit negligible changes in specific capacity. However, after 100 cycles, significant capacity fading is observed in P(VDF-TrFE)-1.03 M, P(VDF-TrFE)-0.60 M, and P(VDF-TrFE)-0.49 M based cells. In contrast, NCM811/P(VDF-TrFE)-2.37 M/Li exhibits only minor attenuation, with a much slower degradation rate, demonstrating that the high-entanglement electrolyte provides superior cycling stability to the full cell. To further analyze the interfacial stability of NCM811/P(VDF-TrFE)/Li cells, EIS were performed after prolonged cycling, as shown in Fig. 5g and S19. All samples exhibited a decrease in interfacial resistance after 100 cycles, indicating the formation of a more favorable SEI. Notably, NCM811//Li cells based on high-M_w P(VDF-TrFE) (2.37 and 1.03 M) show less decrement than low-M_w P(VDF-TrFE) (0.49 M), demonstrating that cells based on high-M_w P(VDF-TrFE) forms stable SEI more quickly than cells based on low-M_w P(VDF-TrFE). The results suggest that the high-entanglement P(VDF-TrFE) electrolyte promotes superior interfacial compatibility and improves the electrochemical stability of the battery during long-term cycling.

The rate capability of NCM811/P(VDF-TrFE)/Li batteries with different molecular weights of P(VDF-TrFE) was evaluated at various charge–discharge rates, as shown in Fig. 5h. The specific discharge capacities of the NCM811/P(VDF-TrFE)-2.37 M/Li at 0.5C, 1C, 2C, and 5C were 155 mAh g^{-1}, 143 mAh g^{-1}, 129 mAh g^{-1}, and 110 mAh g^{-1}, respectively. In comparison, the NCM811/P(VDF-TrFE)-0.49 M/Li displayed rate performance with capacities of only 149 mAh g^{-1}, 138 mAh g^{-1}, 128 mAh g^{-1}, and 106 mAh g^{-1} at the respective charge–discharge rates. Notably, NCM811/P(VDF-TrFE)-2.37 M/Li exhibited excellent capacity retention upon returning to 1C, demonstrating the high reversibility and stability of the SSEs. To further investigate the impact of molecular chain entanglement on the electrochemical stability of NCM811/P(VDF-TrFE)/Li cells, cyclic voltammetry (CV) was performed, as shown in Fig. 5i and S20. The evolution of the reduction peak from the first to the sixth cycle was analyzed for each electrolyte composition. It was observed that the redox peaks of the NCM811/P(VDF-TrFE)-2.37 M/Li cell exhibited minimal shifts and strong overlap of peak position across cycles, indicating excellent reversibility. In contrast, the CV curves of the P(VDF-TrFE)-0.49 M and P(VDF-TrFE)-1.03 M cells displayed larger changes in peak position and intensity, suggesting inferior electrode reaction reversibility. The enhanced electrochemical stability of the high-molecular-

weight P(VDF-TrFE)-2.37 M electrolytes can be attributed to its stronger polymer chain interactions due to its high entanglement, which suppresses ion aggregation, reduce side reactions, and provides a more stable electrolyte–electrode interface. These findings further confirm that optimizing the molecular chain entanglement of P(VDF-TrFE) is a critical factor in improving the long-term cycling performance and electrochemical stability of SSLBs.

3. Conclusions

In summary, we have successfully incorporated TrFE into the PVDF matrix through an *in situ* copolymerization strategy, developing a high-polarity polymer electrolyte featuring both an all-trans TTTT conformation and optimized molecular chain entanglement. This innovative design simultaneously addresses multiple critical challenges in SSEs by: (1) enhancing dielectric properties through the stabilized TTTT conformation, (2) improving ionic transport *via* controlled chain entanglement networks, and (3) reinforcing mechanical strength to suppress lithium dendrite growth. The resulting electrolyte system demonstrates exceptional electrochemical stability (>5000 h cycling in symmetric cells) and practical applicability (82.2% capacity retention after 300 cycles in NCM811//Li full cells). This work not only elucidates the synergistic optimization mechanism of molecular weight regulation on the multiscale structure of SSEs, but also provides novel material design principles for developing high-safety and long-life SSLBs.

Author contributions

Hanghua Wu: data curation equal, writing – original draft – equal; Shuangfeng Li: data curation – equal, writing – original draft – equal; Weiwei Zhu: data curation – equal; Jie Zhang: data curation – supporting; Baohui Ren: methodology – lead, supervision – equal, writing – review & editing – equal; Yanfei Huang, PhD: funding acquisition – lead, resources – lead, supervision – lead, writing – review & editing – lead; Zhongming Li: funding acquisition – supporting, writing – review – supporting.

Conflicts of interest

The authors declare no conflict of interest.

Data availability

The data supporting this article have been included as part of the supplementary information (SI). Supplementary information: experimental methods, characterization data. See DOI: **https://doi.org/10.1039/d5sc04743a**.

Acknowledgements

This work acknowledges the financial support from the National Natural Science and Foundation of China (No. U21A2090 and 52373040), the Guangdong Basic and Applied Basic Research Foundation (2023A1515030247 and 2025B1515020068), the Shenzhen Science and Technology Research and Development Fund (JCYJ20220531102013031 and JCYJ20240813142610015), the Shenzhen University 2035 Program for Excellent Research (2023C005), and the Scientific and Technological Innovation Leading Talent Project of Zhejiang Province (2022R52011). This work thanks the Instrumental Analysis Center of Shenzhen University (Lihu Campus) for assistance with the measurement.

References

1 P. Shi, J. Ma, M. Liu, S. Guo, Y. Huang, S. Wang, L. Zhang, L. Chen, K. Yang, X. Liu, Y. Li, X. An, D. Zhang, X. Cheng, Q. Li, W. Lv, G. Zhong, Y.-B. He and F. Kang, *Nat. Nanotechnol.*, 2023, **18**, 602–610.
2 B. Ai, W. Zhao, M. Li, W. Zhang, D. Mei and J. Yu, *J. Am. Chem. Soc.*, 2025, **147**, 11072–11079.
3 S. Guo, Y. Su, K. Yan, C. Zhao, Y. Lu, H. Wang, J. Dong, N. Li, Y. Liu, Y. Guan, F. Wu and L. Chen, *Adv. Sci.*, 2024, **11**, 2404307.
4 S. Liu, L. Zhou, T. Zhong, X. Wu and K. Neyts, *Adv. Energy Mater.*, 2024, **14**, 2403602.
5 J. Shen, M. Zhou, W. Liu, Y. Shi, W. Tang, Y. Deng, R. Liu, Y. Zuo and J. Zhang, *Energy Storage Mater.*, 2025, **74**, 103964.
6 N. Wu, Y. Li, A. Dolocan, W. Li, H. Xu, B. Xu, N. S. Grundish, Z. Cui, H. Jin and J. B. Goodenough, *Adv. Funct. Mater.*, 2020, **30**, 2000831.
7 S. Wang, J. Hu, X. Gui, S. Lin and Y. Tu, *J. Electrochem. Soc.*, 2021, **168**, 020514.
8 T. Dong, H. Zhang, R. Hu, P. Mu, Z. Liu, X. Du, C. Lu, G. Lu, W. Liu and G. Cui, *Energy Storage Mater.*, 2022, **50**, 525–532.
9 C. Hu, Y. Shen, M. Shen, X. Liu, H. Chen, C. Liu, T. Kang, F. Jin, L. Li, J. Li, Y. Li, N. Zhao, X. Guo, W. Lu, B. Hu and L. Chen, *J. Am. Chem. Soc.*, 2020, **142**, 18035–18041.
10 C. Dai, M. Weng, B. Cai, J. Liu, S. Guo, H. Xu, L. Yao, F. J. Stadler, Z.-M. Li and Y.-F. Huang, *Energy Environ. Sci.*, 2024, **17**, 8243–8253.
11 Y. Wu, Y. Li, Y. Wang, Q. Liu, Q. Chen and M. Chen, *J. Energy Chem.*, 2022, **64**, 62–84.
12 J.-P. Zeng, J.-F. Liu, H.-D. Huang, S.-C. Shi, B.-H. Kang, C. Dai, L.-W. Zhang, Z.-C. Yan, F. J. Stadler, Y.-B. He and Y.-F. Huang, *J. Mater. Chem. A*, 2022, **10**, 18061–18069.
13 Y.-F. Huang, J.-P. Zeng, S.-F. Li, C. Dai, J.-F. Liu, C. Liu and Y.-B. He, *Adv. Energy Mater.*, 2023, **13**, 2203888.
14 P. Zhai, Z. Yang, Y. Wei, X. Guo and Y. Gong, *Adv. Energy Mater.*, 2022, **12**, 2200967.
15 Z. Jia, M. Jia, Q. Sun, N. Wang, Z. Bi and X. Guo, *Energy Storage Mater.*, 2024, **68**, 103325.
16 S. Zhang, F. Sun, X. Du, X. Zhang, L. Huang, J. Ma, S. Dong, A. Hilger, I. Manke, L. Li, B. Xie, J. Li, Z. Hu, A. C. Komarek, H.-J. Lin, C.-Y. Kuo, C.-T. Chen, P. Han, G. Xu, Z. Cui and G. Cui, *Energy Environ. Sci.*, 2023, **16**, 2591–2602.
17 Y. Jin, X. Zong, X. Zhang, Z. Jia, H. Xie and Y. Xiong, *Energy Storage Mater.*, 2022, **49**, 433–444.

18 Y.-L. Liao, X.-L. Wang, H. Yuan, Y.-J. Li, C.-M. Xu, S. Li, J.-K. Hu, S.-J. Yang, F. Deng, J. Liu and J.-Q. Huang, *Adv. Mater.*, 2025, **37**, 2419782.
19 Y. Wu, Z. Chen, K. Shi, Y. Wang, X.-A. Li, Z. Zhao, Q. Zhuang, J. Wang and M. Chen, *Energy Environ. Sci.*, 2025, **18**, 2817–2825.
20 Q. Liu, G. Yang, X. Li, S. Zhang, R. Chen, X. Wang, Y. Gao, Z. Wang and L. Chen, *Energy Storage Mater.*, 2022, **51**, 443–452.
21 S. Wang, C. Li, Y. Ma, H. Zhang, X. Shi, L. Zhang and D. Song, *Angew. Chem., Int. Ed.*, 2025, **64**, e202420698.
22 Z. Ji, Z. Zhu, A. Ye, J. Yang, W. Cai, G. Wen, S. Yuan, C. Ma, X. Fu, W. Yang and Y. Wang, *Energy Storage Mater.*, 2025, **75**, 104005.
23 X. An, Y. Liu, K. Yang, J. Mi, J. Ma, D. Zhang, L. Chen, X. Liu, S. Guo, Y. Li, Y. Ma, M. Liu, Y.-B. He and F. Kang, *Adv. Mater.*, 2024, **36**, 2311195.
24 Y. Lee, V. K. Bandari, V. P. Paliakkara, S. Monteiro Augusto, R. Ehrler, O. Hellwig, S. Amann, K. Stöwe, R. Thalheim and O. G. Schmidt, *Adv. Funct. Mater.*, 2025, **35**, 2413500.
25 N. A. Shepelin, P. C. Sherrell, E. N. Skountzos, E. Goudeli, J. Zhang, V. C. Lussini, B. Imtiaz, K. A. S. Usman, G. W. Dicinoski, J. G. Shapter, J. M. Razal and A. V. Ellis, *Nat. Commun.*, 2021, **12**, 3171.
26 D. Xu, S. Fu, H. Zhang, W. Lu, J. Xie, J. Li, H. Wang, Y. Zhao and R. Chai, *Adv. Mater.*, 2024, **36**, 2307896.
27 H. Hattori, T. Watanabe, S. Akama, M. Hikosaka and H. Ohigashi, *Polymer*, 1997, **38**, 3505–3511.
28 Y. Huang, G. Rui, Q. Li, E. Allahyarov, R. Li, M. Fukuto, G.-J. Zhong, J.-Z. Xu, Z.-M. Li, P. L. Taylor and L. Zhu, *Nat. Commun.*, 2021, **12**, 675.
29 H. Kim, J. Kim, J. Lee, M. Lee, M. K. Kim, S. Ahn, J. Kim, J. Jin and S. J. Kang, *Energy Storage Mater.*, 2024, **67**, 103260.
30 L. Deng, J.-K. Liu, Z. Wang, J.-X. Lin, Y.-X. Liu, G.-Y. Bai, K.-G. Zheng, Y. Zhou, S.-G. Sun and J.-T. Li, *Adv. Energy Mater.*, 2024, **14**, 2401514.
31 S. Wang, J. Yang, W. Cai, G. Wen, S. Yang, K. Ke, B. Yin, X. Fu, W. Yang and Y. Wang, *Adv. Energy Mater.*, 2024, **14**, 2401937.
32 Y. Yang, F. Duan, X. Yao, Z. Xuan, X. Chen, M. Shi, Z. Chen, T. Huang, Y. Chen and Y.-Q. Lan, *Adv. Mater.*, 2025, 2505206.
33 Y. Huang, J.-Z. Xu, T. Soulestin, F. D. Dos Santos, R. Li, M. Fukuto, J. Lei, G.-J. Zhong, Z.-M. Li, Y. Li and L. Zhu, *Macromolecules*, 2018, **51**, 5460–5472.
34 H. Wang, Y. Yang, C. Gao, T. Chen, J. Song, Y. Zuo, Q. Fang, T. Yang, W. Xiao, K. Zhang, X. Wang and D. Xia, *Nat. Commun.*, 2024, **15**, 2500.
35 R. Bu, B. Zhang, D. Li, H. Cheng, Q. Ruan, W. Zhong, C. Tan, Y. Wang, J. Zhang, B. Chen, C. Liu, E.-Q. Gao and Y. Lu, *Adv. Funct. Mater.*, 2025, e12777.
36 D. Wang, B. Jin, J. Huang, X. Yao, Y. Ren, X. Xu, X. Han, F. Li, X. Zhan and Q. Zhang, *ACS Appl. Mater. Interfaces*, 2023, **15**, 32385–32394.
37 C. Ye, T. Yang, Z. Li, S. Zhao, Z. Liu, D. Kang, J. Zhou, J. Li and Z. Xin, *Mater. Lett.*, 2023, **349**, 134783.
38 Y.-F. Huang, T. Gu, G. Rui, P. Shi, W. Fu, L. Chen, X. Liu, J. Zeng, B. Kang, Z. Yan, F. J. Stadler, L. Zhu, F. Kang and Y.-B. He, *Energy Environ. Sci.*, 2021, **14**, 6021–6029.
39 T. Furukawa, *Adv. Colloid Interface Sci.*, 1997, **71–72**, 183–208.
40 Y. Li, T. Soulestin, V. Ladmiral, B. Ameduri, T. Lannuzel, F. Domingues Dos Santos, Z.-M. Li, G.-J. Zhong and L. Zhu, *Macromolecules*, 2017, **50**, 7646–7656.
41 Z. Li, J. Fu, X. Zhou, S. Gui, L. Wei, H. Yang, H. Li and X. Guo, *Adv. Sci.*, 2023, **10**, 2201718.
42 G. Feng, Q. Ma, D. Luo, T. Yang, Y. Nie, Z. Zheng, L. Yang, S. Li, Q. Li, M. Jin, X. Wang and Z. Chen, *Angew. Chem., Int. Ed.*, 2025, **64**, e202413306.
43 Y. Li, T. Soulestin, V. Ladmiral, B. Ameduri, T. Lannuzel, F. Domingues Dos Santos, Z.-M. Li, G.-J. Zhong and L. Zhu, *Macromolecules*, 2017, **50**, 7646–7656.
44 Z. Zhu, G. Rui, R. Li, H. He and L. Zhu, *Macromolecules*, 2021, **54**, 9879–9887.
45 H. Yang and N. Wu, *Energy Sci. Eng.*, 2022, **10**, 1643–1671.
46 B. Yang, C. Deng, N. Chen, F. Zhang, K. Hu, B. Gui, L. Zhao, F. Wu and R. Chen, *Adv. Mater.*, 2024, **36**, 2403078.
47 W. Yang, Y. Liu, X. Sun, Z. He, P. He and H. Zhou, *Angew. Chem., Int. Ed.*, 2024, **63**, e202401428.
48 N. Wang, M. Jia, Z. Bi and X. Guo, *Adv. Funct. Mater.*, 2024, **34**, 2401400.
49 Y. Xu, K. Wang, X. Zhang, Y. Ma, Q. Peng, Y. Gong, S. Yi, H. Guo, X. Zhang, X. Sun, H. Gao, S. Xin, Y.-G. Guo and Y. Ma, *Adv. Energy Mater.*, 2023, **13**, 2204377.
50 X. Zhang, J. Han, X. Niu, C. Xin, C. Xue, S. Wang, Y. Shen, L. Zhang, L. Li and C.-W. Nan, *Batteries Supercaps*, 2020, **3**, 876–883.
51 N. Vallana, E. Carena, N. Ceribelli, L. Mezzomo, G. Di Liberto, M. Mauri, C. Ferrara, R. Lorenzi, L. Giordano, R. Ruffo and P. Mustarelli, *ACS Appl. Energy Mater.*, 2024, **7**, 1606–1617.
52 Y.-X. Yao, X. Chen, C. Yan, X.-Q. Zhang, W.-L. Cai, J.-Q. Huang and Q. Zhang, *Angew. Chem., Int. Ed.*, 2021, **60**, 4090–4097.
53 W. Liu, C. Yi, L. Li, S. Liu, Q. Gui, D. Ba, Y. Li, D. Peng and J. Liu, *Angew. Chem., Int. Ed.*, 2021, **60**, 12931–12940.
54 G. Liu, R. G. Larson, L. Li, H. Luo, X. He, Y. Niu and G. Li, *Macromolecules*, 2023, **56**, 2719–2728.
55 Y. Kamiyama, R. Tamate, T. Hiroi, S. Samitsu, K. Fujii and T. Ueki, *Sci. Adv.*, 2022, **8**, eadd0226.
56 T. Dong, J. Zhang, G. Xu, J. Chai, H. Du, L. Wang, H. Wen, X. Zang, A. Du, Q. Jia, X. Zhou and G. Cui, *Energy Environ. Sci.*, 2018, **11**, 1197–1203.
57 G. Xu, M. Zhao, B. Xie, X. Wang, M. Jiang, P. Guan, P. Han and G. Cui, *J. Power Sources*, 2021, **499**, 229944.
58 X. Zhang, J. Han, X. Niu, C. Xin, C. Xue, S. Wang, Y. Shen, L. Zhang, L. Li and C.-W. Nan, *Batteries Supercaps*, 2020, **3**, 876–883.